Dalton Transactions

PAPER

View Article Online
View Journal | View Issue

Cite this: *Dalton Trans.*, 2026, **55**, 1149

Unveiling the structural and electrochemical effects of Al_2O_3 incorporation within LiPON electrolyte thin films by atomic layer deposition

Ilyass Ghandari, *[a] Nicolas Gauthier,[a] Névine Rochat,[a] Sylvain Poulet,[a] Lara Casiez,[a] Manon Letiche,[a] Violaine Salvador,[a] Hélène Coudert-Alteirac,[a] Nicolas Vaxelaire,[a] Mikhael Bechelany [b] and Messaoud Bedjaoui*[a]

Received 29th October 2025,
Accepted 11th December 2025

DOI: 10.1039/d5dt02597d

rsc.li/dalton

Thin film solid-state electrolytes (SSEs) have emerged as a key component in the development of microenergy storage devices, offering improved safety, stability and compatibility with advanced electrode materials. Among these electrolytes, lithium phosphorus oxynitride (LiPON) stands out as a relevant SSE candidate for microsupercapacitor applications. As with most ionic conductors, a margin for improvement always exists to enhance their overall performance. Within this scope, efforts to optimize LiPON through doping have been extensively explored, primarily using Physical Vapour Deposition (PVD) to provide films with relatively high thicknesses (500 nm–1 μm) and superior ionic conductivity. In this study, the use of Atomic Layer Deposition (ALD) for doping LiPON thin films (<50 nm) was explored for the first time, by inserting aluminum oxide (Al_2O_3) as a network former. Through the ALD supercycle approach, Al_2O_3 doped-LiPON thin films were deposited at 330 °C, using lithium hexamethyldisilazide (LiHMDS) and diethyl phosphoramidate (DEPA), while Al_2O_3 traces were injected during the film growth *via* trimethylaluminum (TMA) and water (H_2O) pulses. The resulting amorphous films were depth profiled by Time of Flight Secondary Ion Mass Spectrometry (ToF-SIMS) and demonstrated a uniform distribution of aluminium throughout the film's thickness for different doping levels. The incorporation of Al_2O_3 is intended to enable additional Li^+ transport pathways through modified bridging configurations, particularly in oxygen and nitrogen environments. The Fourier transform infrared spectroscopy (FTIR) analysis indicated a prevalence of Bridging Oxygen (BO) and divalent nitrogen (N_d) units upon doping. These findings were further supported by X-ray photoelectron spectroscopy (XPS), underlining an increase in the ratios of Bridging Oxygen to Non-Bridging Oxygen (BO/NBO) and divalent nitrogen to trivalent nitrogen (N_d/N_t) along with higher lithium and lower carbon concentrations. The obtained structural modifications were accompanied by a stimulated Li^+ ionic transport and a reduced activation energy, while maintaining a good insulating property and an electrochemical stability over a wide voltage window (up to 6 V).

1. Introduction

Nowadays, the rapid progress in integrated passive solutions is driven by the growing quest for efficient energy storage devices with enhanced performance and innovative functionalities.[1] In several domains ranging from medical wearable electronics to IoT applications, efficient energy storage components, such as micro-supercapacitors (MSCs), play a crucial role in stabilizing power supplies, reducing noise and improving system reliability.[1,2] As a result, MSCs become indispensable for powering wireless device networks deployed in diverse domains, including industrial settings, environmental and health monitoring.[3] These components rely on efficient energy storage to enable long-term operation and smooth operations of sensitive electronic components, enabling real-time monitoring and excellent decision-making.[4,5]

The growing demand for increased functionalities and enhanced energy storage is calling for advanced solid-state materials and novel technological approaches.[6,7] In MSCs, solid-state electrolyte (SSE) materials have garnered significant interest due to their potential to optimize energy storage systems. Unlike conventional liquid electrolytes, SSE materials offer multiple advantages such as enhanced safety and stability. In contrast to standard liquid electrolyte systems, SSE materials and their solid-phase analogues require novel

---

[a] *Univ. Grenoble Alpes, CEA LETI, 38054 Grenoble, France.*
E-mail: ilyass.ghandari@cea.fr, messaoud.bedjaoui@cea.fr
[b] *Institut Européen des Membranes-IEM, Univ. Montpellier, CNRS, ENSCM, 34095 Montpellier, France*

approaches in fabrication and integration.[8,9] This necessitates advanced microfabrication techniques that can precisely deposit SSE materials within MSC structures.[10]

In this regard, lithium phosphorus oxynitride (LiPON) appears as a promising SSE, offering excellent properties such as high thermal stability (up to 500 °C) and chemical robustness,[11] minimizing problems at electrode–electrolyte interfaces and improving device lifetime.[12] Moreover, its large potential stability window (0–5 V *vs.* Li/Li^+) enables great suitability for a variety of electrode materials, promoting its versatility in device design.[13]

In the previous years, an intensive scientific research has been achieved to widely investigate thin film deposition techniques, examine suitable deposition conditions and study efficient pathways to enhance LiPON's electrochemical performances.[11] Thus, several explorations on amorphous LiPON films have focused on improving ionic conductivity. In this context, doping and network rearrangements become well-established approaches for improving lithium ion migration pathways within the SSE films.[14] Multiple cation dopings, such as Al^{3+}, Ti^{2+}, Fe^{3+} *etc.* have demonstrated interesting pathways to generate rearrangements in LiPON's structure and facilitates Li^+ mobility.[14–16] For example, the doping of iron (Fe) in LiPON led to an excellent ionic conductivity (~10^{-5} S cm^{-1}). The insertion of iron cations allowed local alteration of the electron density in LiPON's matrix and reducing the energy barrier to Li^+ migration near the Fe–N bridges.[16] A previous research by Yurong Su *et al.*[17] has explored structural comparisons between LiPON and Li(Si)PON. They have shown that the incorporation of silicon induced increased rearrangement in the chemical structure of LiPON, with a significant improvement in the cross-linking of oxygen environment, enabling an improved ionic conductivity.[17]

Despite these extensive doping approaches on LiPON electrolyte, most of these films were deposited by PVD (Physical Vapor Deposition) and exceeded 1 μm thickness, which is limiting their utility when applied to nanoscale devices and non-planar architectures.[18] This highlights a crucial technological need for suitable doping strategies targeting LiPON ultra-thin films (<50 nm) and compatible with complex geometries. In this regard, ALD offers an unparalleled control over the film thickness and the composition at the atomic scale, enabling the deposition of ultrathin and highly conformal films on 3D microstructures.[19,20] Hence, investigating ALD approaches for doping LiPON films can open new possibilities for depositing nanoscale solid electrolytes and improving their ionic conductivities.

The earliest ALD LiPON films were deposited in 2015 by C. Kozen *et al.*[21] and by M. Nisula *et al.*[22] Meanwhile, different thermal ALD processes have been developed to deposit the amorphous LiPON films based on different combinations of precursors such as lithium bis (trimethylsilyl)amide (LiHMDS) or lithium *tert*-butoxide (LiO*t*Bu) with nitrogen, oxygen and phosphorus precursors such as diethylphosphoramidate (DEPA) or tris(dimethylamino)phosphine (TDMAP).[13,23,25]

Nowadays, these prior efforts are providing solid foundations on LiPON deposited *via* ALD, enabling us to initiate further studies on modifying and improving LiPON's internal structure by incorporating complementary materials. In this sense, the insertion of oxides is commonly recognized as advantageous to the use of non-oxidized materials (*e.g.*, sulfides, halides, noble metals) due to the ease of handling, the chemical and electrochemical stability these oxide materials.[26] Additionally, the insertions of nanoscale fillers such as TiO_2, SiO_2, WO_3 *etc.* have showed excellent ability to induce chemical substitutions and improve ionic conductivity in various SSE.[27,28] Among these materials, aluminum oxide (Al_2O_3) holds a distinguished position in both SSE and ALD fields.

Al_2O_3 has been widely employed as a protective coating for Li anodes,[29] or as an interfacial layer with SSE in thin film batteries,[30] helping to suppress parasitic reactions and enhancing the cycle life. Additionally, ALD-enabled phosphate-based materials, such as aluminum phosphate ($AlPO_4$)[31] and aluminophosphate oxynitride (AlPON),[32] have shown significant promise as Li-conducting materials due to their excellent thermal stability and high resistance to corrosion. In other applications, Hong Dong *et al.*[33] investigated the incorporation of LiPON traces within Al_2O_3 films *via* ALD, leading to an enhanced dielectric constant thanks to the additional Li^+ mobility. This work also demonstrates the suitability of combining LiPON and Al_2O_3 within the same ALD process, particularly in terms of deposition temperature and chemical compatibility, as both materials can be deposited within a similar range (~300 °C) without adverse interactions. However, the use of Al_2O_3 in thin-film SSE synthesis remains relatively unexplored, and Al_2O_3-doped LiPON has not yet been explored as a thin film electrolyte. Being a highly insulating material,[34] Al_2O_3 would be favorably integrated into the LiPON matrix without compromising its electrical insulating properties. Moreover, the incorporation of Al^{3+} cations can easily induce structural rearrangements within the phosphate network,[35] altering the local electronic environment around lithium ions and reducing their migration barriers. Furthermore the well-understood ALD growth mechanism of alumina and its ability to form highly conformal films on complex surfaces,[36,37] makes it an ideal candidate for doping films within 3D geometries and suitable for the next generation of nano-energy storage devices.

The aim of our investigation was to study the chemical and structural changes associated with the Al_2O_3 incorporation within LiPON matrix and establish deeper understandings on the synergy between compositional factors and Li^+ mobility within LiPON-doped thin films. For instance, we firstly aimed to develop the optimal ALD conditions, enabling appropriate insertion of Al_2O_3 trace amount within LiPON without compromising its ionic functionalities as a solid electrolyte. The physico-chemical characteristics were systematically monitored based on multiple complementary techniques, including X-ray Photoelectron Spectroscopy (XPS), Time-of-Flight Secondary Ion Mass Spectrometry (ToF-SIMS), Fourier Transform Infrared Spectroscopy (FTIR), and X-ray Diffraction (XRD). Furthermore, the electrochemical behavior was evaluated through Cyclic

Voltammetry (CV), Electrochemical Impedance Spectroscopy (EIS) and Chronoamperometry (CA) to assess variations in ionic conductivity, insulating behavior and electrochemical stability window. The results revealed that aluminum insertion significantly influenced the oxygen and nitrogen atomic environments within the LiPON matrix while also increasing the lithium content. These intrinsic rearrangements led to a progress in ionic conductivity and decrease in activation energy, without altering the insulating properties and the electrochemical stability of the films.

2. Experimental section

2.1. Film deposition

The LiPON and LiAlPON doped films were deposited by atomic layer deposition (ALD) on 200 mm silicon wafers using PicoSun R200 Advanced reactor, from Applied Materials. The deposition process used Lithium bis (trimethylsilyl) amide (LiHMDS, Sigma Aldrich purity 97%) as lithium source, and Diethylphosphoramidate (DEPA, Sigma Aldrich purity 98%) as phosphorus, oxygen and nitrogen source. Both precursors were stored in stainless steel bubblers maintained at specific temperatures: LiHMDS at 60 °C and DEPA at 90 °C, to reach the required vapor pressure. The deposition process was carried out at 330 °C, with argon used as both the carrier and purging gas, flowing at a rate of 120 standard cubic centimeters per minute (sccm). The Al_2O_3 doping traces were incorporated by Trimethylaluminum (TMA) and water (H_2O), which were stored in stainless steel tank containers, set at room temperature (25 °C). As illustrated in Fig. 1, the LiPON doped films were grown using a supercycle approach to vary the concentration of Al_2O_3 within the LiPON films.

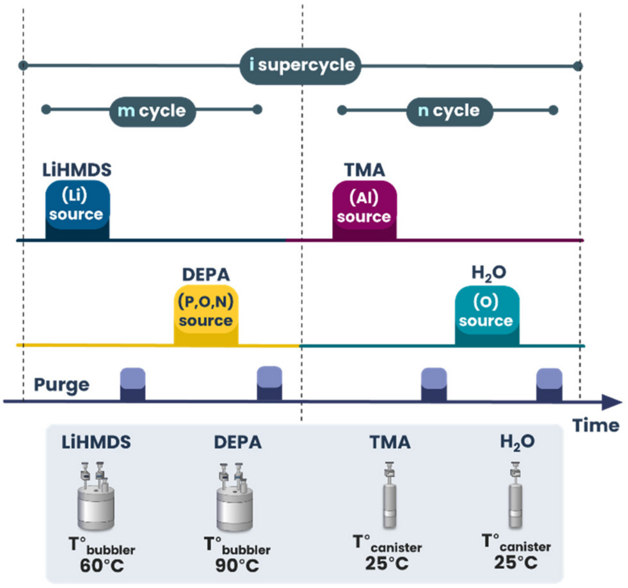

Fig. 1 Schematic representation of ALD supercycles used to modify the LiPON films with Al_2O_3 doping element.

2.2. Physico-chemical characterization

Thickness measurements were performed for LiPON and LiAlPON doped films deposited on planar Si/SiO_2 using a Woolam RC2 spectroscopic ellipsometer. A Cauchy optical model was applied to extract the thickness of both undoped and doped LiPON films after deposition. Spectroscopic ellipsometry was performed over a wavelength range of 210–2500 nm. The error bars associated with the reported thickness values arise from the propagation of uncertainties in the optical model, resulting in a measurement accuracy between ±0.5 and ±1 nm. A short air exposure was required during sample transfer before the analysis. The film was additionally evaluated by scanning electron microscopy (SEM) on TiN-coated Si 3D structures. The images were acquired using a ZEISS Ultra 55 at a beam energy of (EHT = 3 kV, WD = 3.3 mm, magnification = 29.95 and magnification = 58). X-ray diffraction (XRD) was utilized to highlight the microstructure of the films. XRD analysis was carried out on LiPON, LiAlPON and Al_2O_3 films (~30 nm) deposited on planar $Si/SiO_2/TiN$ substrate, using a Panalytical EMPYREAN X1 diffractometer with a Cu Kα X-ray source. The measurements were performed in grazing incidence geometry in order to maximize the diffraction signal from the thin layers. Time-of-Flight Secondary Ion Mass Spectrometry (ToF-SIMS) measurements were performed on LiPON and LiAlPON doped films (~30 nm) deposited on planar $Si/SiO_2/TiN$ substrates, using a ToF-SIMS 5 Instrument, from ION TOF GmbH equipped with Bismuth-LMIG. To prevent air exposure, all samples were transferred in an airtight vessel. For secondary ions analysis, the LMIG gun was tuned to deliver primary Bi_3^+ cluster ions energized at 30 kV and with a current of 6.2 pA currents. The analysis area of 75 × 75 μm^2 is described in 128 × 128 pixels for positive and negative polarity secondary ions. The depth analyses were carried out with an Argon Gas Cluster Ion Beam (for etching): the surface was sputtered with 10 keV Ar_{1030}^+ clusters ions with an 8 nA current and a raster size of 300 × 300 μm^2. Data treatment was carried out with the SurfaceLab software. Attenuated total reflectance Fourier transform infrared (ATR–FTIR) spectroscopy measurements were performed inside an N_2-filled environmental chamber. The measurements were carried out using Vertex 70A spectrometer on samples consisting of ~30 nm film thickness deposited on Si substrate to reduce the SiO_2 substrate contributions. The ATR accessory equipped with Ge crystal was used to record ATR–FTIR spectra. The FTIR spectra were averaged over 200 scans with a spectral resolution of 4 cm^{-1} in the 2800–600 cm^{-1} region. X-ray Photoelectron Spectroscopy (XPS) analysis was carried out on LiPON and LiAlPON doped films (~30 nm) deposited on planar Si/SiO_2 with ULVAC-PHI Versa Probe II spectrometer. To prevent air exposure, all samples were transferred to the XPS tool in an airtight vessel (PHI Transfer Vessel). Measurements were performed under ultra-high vacuum ($P_{chamber} < 5 \times 10^{-7}$ Pa) with a micro focused (beam size diameter of 100 μm) Al Kα X-ray beam (photon energy of 1486.6 eV), and a take-off angle of 45°. Argon gas cluster ion beam etching (GCIB) was carried out in order to remove surface contamination without damaging the structure and to have access to the bulk chemical structure. A cluster size of 2500 atoms accelerated to 10 kV with a current of 5 nA was employed. Peak fitting was carried out using the CasaXPS data analysis software and the binding energies of all elements were calibrated based on the C 1s peak set to 285.0 eV. We note that due to experimental constraints and the specific requirements of each characterization technique, substrates were adapted. We expect that the LiPON composition is not significantly influenced by the choice of substrate.

2.3. Electrochemical analysis

For the test vehicle fabrication, a 10 nm TiN layer was first deposited on planar Si/SiO_2 wafers by ALD using a Picosun PICOPLATFORM system with titanium tetrachloride ($TiCl_4$) and ammonia (NH_3) precursors at 400 °C. LiPON-based films were then deposited by thermal ALD using a Picosun R200 tool. Finally, platinum electrodes were patterned by evaporation (EVAP1005) through a shadow mask, preceded by a brief Ar pre-cleaning (~10 s), forming rectangular electrodes with an area of 2 mm^2. This process yields several identical in-plane MIM structures, enabling multiple measurements and ensuring reproducibility. Electrochemical Impedance Spectroscopy (EIS) measurements were performed using a VMP3 multipotentiostat (Bio-Logic) coupled with the EC-Lab software to measure the internal resistance and extract the ionic conductivity of the films. Cyclic Voltammetry (CV) was conducted using the same setup to determine the potential stability window of the films. Additional EIS measurements were performed on the deposited films samples at a range of temperatures between 25 and 75 °C to determine the activation energy. A temperature-controlled climatic chamber was employed to bring the samples to the desired temperatures. It should be noted that although all possible precautions were taken to control and minimize air contact, LiPON films were unavoidably exposed to air during handling and throughout electrochemical measurements.

3. Results and discussion

3.1. ALD process development

The thermal ALD of LiPON is based on a bi-step process of LiHMDS-DEPA at 330 °C, with the precursor saturation doses of 4 s for LiHMDS and 2 s for DEPA, as established in our previous study of LiPON ALD.[24] The precursor cycling led to a linear regime according to the self-limiting growth behavior and resulted in a GPC of approximately 0.4 Å per cycle (Fig. 2). Additionally, aluminum oxide films were deposited using cycles of TMA (0.1 s)–H_2O (0.1 s) at 330 °C, resulting in a GPC of 0.9 Å per cycle (Fig. 2). To incorporate aluminum atoms within LiPON films, a supercycle approach was employed, in which (LiHMDS-DEPA) cycles were sequentially separated by single injections of TMA–H_2O. Through this approach, we aimed to vary the aluminum concentrations by adjusting the ratio of LiPON to Al_2O_3 cycles within each supercycle.

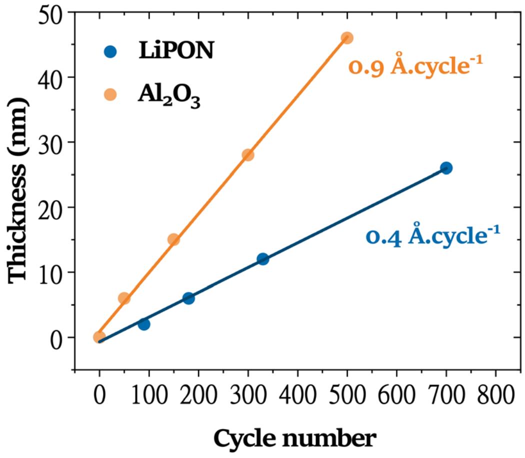

Fig. 2 The thickness progression as a function of ALD cycle number for LiPON (blue dots) and Al_2O_3 (orange dots) deposited at 330 °C.

Combining these two different materials within a supercycle approach, can lead to potential interferences in their inherent growth behaviors.[35,38] Hence, it is vital to assess the compatibility of the supercycle method with the rule of mixtures (ROM), described mathematically as follows.[38,39]

Rule of mixtures:

$$\text{Thickness} = i \times (m \times \text{GPC}_{(\text{LiPON})} + n \times \text{GPC}(_{\text{Al}_2\text{O}_3}))$$

Here, GPC refers to the growth per cycle of the pure materials (LiPON and Al_2O_3), i refers to number of supercycles, while m and n are the respective cycle counts for LiPON and Al_2O_3 in one supercycle.

To evaluate whether the growth behavior of the doped films aligns with the linear combination expected by the ROM, we measured the film thicknesses as a function of the supercycle number. In Table 1, we summarized the number of LiPON and Al_2O_3 cycles per supercycle, the total number of supercycles and the measured thicknesses by ellipsometry. From Fig. 3(a)–(c), the thicknesses measured by ellipsometry demonstrate a linear evolution. For the 1 : 20 supercycle sequence, the experimental thicknesses are slightly higher than the calculated values, while the 10 : 1 and 1 : 1 supercycles exhibit a good agreement with the theoretical thicknesses. Overall, these linear increases in thicknesses suggest that LiPON and Al_2O_3 growth are potentially independent from each other and the insertion of Al_2O_3 may not induce significant nucleation delay or alteration during LiPON growth.[38]

Table 1 Supercycle parameters and resulting film thicknesses for LiPON and LiAlPON thin films

Films	LiPON cycles	Al_2O_3 cycles	Super cycles	Thickness (nm)
LiPON	700	0	—	26
$\text{LiAlPON}_{(20:1)}$	20	1	23	24
$\text{LiAlPON}_{(10:1)}$	10	1	55	25
$\text{LiAlPON}_{(1:1)}$	1	1	200	26

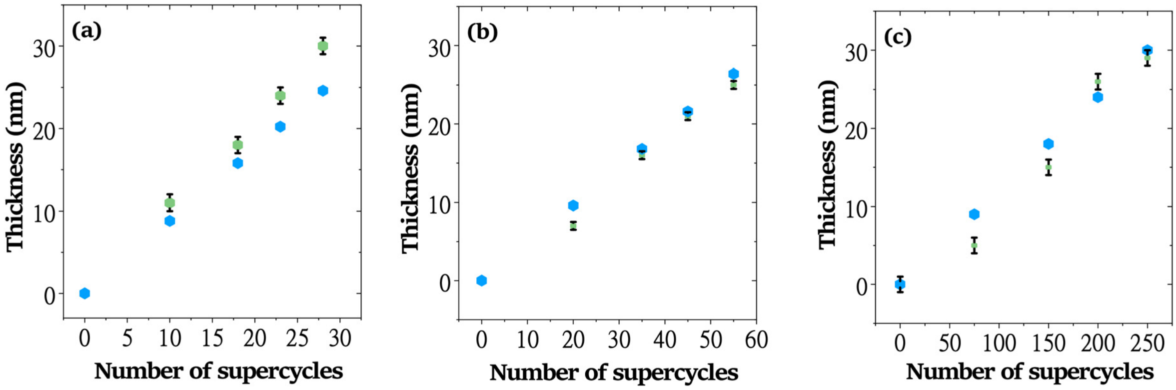

Fig. 3 Comparison of calculated (blue dots) and measured (green dots) thicknesses of LiPON doped films (on planar substrate) as a function of supercycle number for (a) $LiAlPON_{(20:1)}$, (b) $LiAlPON_{(10:1)}$ and (c) $LiAlPON_{(1:1)}$.

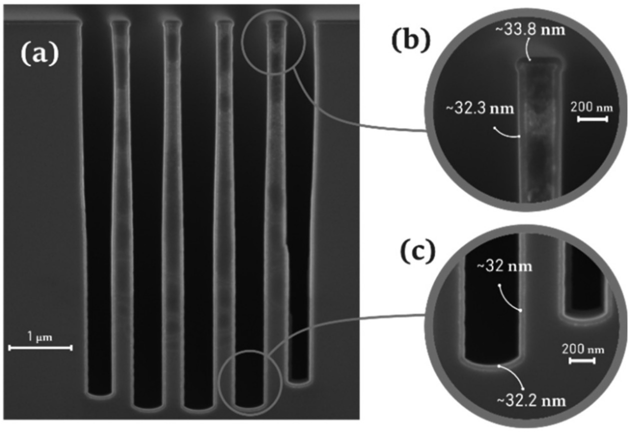

Fig. 4 SEM imaging of the thin film deposited within a 3D structure using a supercycle ALD process of $LiAlPON_{(20:1)}$ on TiN film (~10 nm). (a) Micropillars of 5 µm of high and 500 nm of diameter were employed. (b) Image from top position (c) image from bottom position.

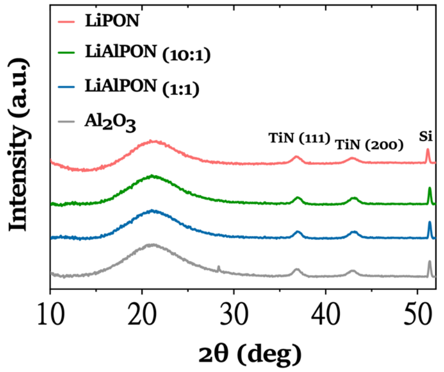

Fig. 5 Comparison of GI-XRD profiles on planar substrate for LiPON, LiAlPON, and Al_2O_3 films.

Complementary SEM imaging on 3D structures was performed to gain additional insights into the film (Fig. 4). As an example, the $LiAlPON_{(20:1)}$ process was performed on a 3D microstructure (5 µm height, 500 nm diameter), previously coated with a ~10 nm TiN layer (by ALD). The film demonstrated globally a uniform and continuous coating across all locations of the micropillar surfaces. Considering the measured thicknesses at the top (~33.8 nm) and bottom (~32.3 nm) of the 3D structure (Fig. 4(b) and (c)), the step coverage is estimated to be ~95%. Such conformal coverage supports the potential integration of these films into more complex geometries with higher aspect ratios required for high power density applications.

3.2. Thin film characterization

The material microstructure was analyzed by GI-XRD to highlight the amorphous nature of the thin films, verifying that the Al_2O_3 incorporation preserves a favorable amorphous structure, which is a key characteristic for achieving excellent electrochemical performance.[40] The XRD patterns of the LiPON-based film deposited at various doping concentrations are shown in Fig. 5. The samples exhibit a typical bell-shape peak phase around 20° assigned to the long-range disordered amorphous structure of LiPON and Al_2O_3.[41,42] Two additional diffraction peaks were recorded around 37° and 42°, referring to TiN (111) and TiN (200) reflections respectively from the bottom layer.[43]

Depth profile characterization, ToF-SIMS analysis. A uniform distribution of doping agents in LiPON films is typically intended to create homogeneous chemical rearrangements and optimize readjustments of the local electron density in the amorphous network.[16] By sequentially injecting TMA–H_2O pulses during LiPON growth, we expect an excellent repartition of aluminum in the local structure of the film. To explore the elemental distribution of atoms comprised across the films, we performed a depth profiling by TOF-SIMS Fig. S1 (SI) on LiPON, $LiAlPON_{(10:1)}$ and $LiAlPON_{(1:1)}$ films, with a thickness of ~30 nm each, deposited on TiN thin film. We focused our analysis on monitoring the negative ion fragments of interest: $^{6}Li^{-}$, $^{18}O^{-}$, P^{-}, Al^{-}, and TiO^{-}.

While no significant traces of aluminum fragments were detected in LiPON (Fig. S1(a)), the presence of Al^{-} ions was noticed in the bulk of $LiAlPON_{(1:10)}$ film (Fig. S1(b)) and a superior intensity level was observed for $LiAlPON_{(1:1)}$ film (Fig. S1(c)). Furthermore, the aluminum signal displayed a steady repartition within the entire thickness until reaching the interface with the bottom layer (TiN). This reflects the effectiveness of the super-cycle approach, to insert homogeneously Al_2O_3 into the LiPON matrix. Additionally, the intensity levels of phosphorus, lithium and oxygen showed a relatively stable plateau within each film, supporting the uniform distribution of LiPON elements within the film structure.

Chemical structure, FTIR analysis. The local structure of LiPON, $LiAlPON_{(10:1)}$, $LiAlPON_{(1:1)}$ and Al_2O_3 films, has been studied by ATR-FTIR spectroscopy. Fig. 6 shows FTIR spectra of the films deposited on Si substrates measured from 600 cm^{-1} to 2800 cm^{-1} as shown in Fig. S2 (SI). The major peak from each spectrum was deconvoluted using a Gaussian fit with OriginLab software.[44] The reduced statistical coefficient (R^2) values were close to 1 indicating good agreement and that the regression line fits the data perfectly.

For LiPON film (Fig. 6(a)), a major absorbance band is observed between 900 and 1300 cm^{-1}, which corresponds to phosphate-based groups.[45] This band is resolved within three distinct peaks : P–O–P/P–N=P (950–1000 cm^{-1}), PO_3 (1050–1100 cm^{-1}) and P=O (1150–1200 cm^{-1}).[44,46] An additional peak with low-intensity is recorded between the 750–850 cm^{-1}, corresponding P–O–P sequences.[45]

Furthermore, pristine aluminum oxide was analyzed to reveal characteristic functional groups present in Al_2O_3 thin film (Fig. 6(d)). The main IR-band appeared between 600 and 1000 cm^{-1}. This band displays three peaks around 700 cm^{-1} and 800 cm^{-1} which are assigned to Al–O and Al–O–H groups.[47] The more intense peak observed between 850 and 1000 cm^{-1} mainly originates from Al–O and O–H deformation vibrations.[47,48] By incorporating Al_2O_3 into LiPON, the PO_3 and P=O peaks in $LiAlPON_{(10:1)}$ appear relatively unaffected (Fig. 6(b)), while an increase in the right shoulder of the phosphate band indicates enhanced content of P–O–P/P=N–P linkages. However, no distinct aluminum-related peak was noticed, possibly due to the low concentration of aluminum atoms in this configuration. At higher doping ratio, $LiAlPON_{(1:1)}$ (Fig. 6(c)), a clearer peak originating from aluminum species (Al–O–P/Al–O) emerges between 700–800 cm^{-1}, indicating an effective insertion of aluminum within the LiPON matrix. In contrast to $LiAlPON_{(10:1)}$, the P–O–P/P=N–P peak in $LiAlPON_{(1:1)}$ film has diminished, which indicates a possible inverse structural rearrangement trend at higher Al_2O_3 concentrations. R. Blomme *et al.*[49] have observed comparable structural variation in aluminum phosphate films, where the right shoulder of the main phosphate band decreased for high Al_2O_3 content. The variation of P–O–P/P=N–P linkages indicates that the presence of Al_2O_3 within the LiPON bulk has effectively influenced the local environment of phosphate groups. Hence, the chemisorption of TMA and H_2O molecules, can favorably stimulate the formation of new crosslinks and enhances the presence of P–O–P and Al–O–P sequences within the LiPON matrix.[35,50] To gain greater insights, we investigated the atomic environments of each element (Li, P, O and N) of LiPON using XPS analysis.

Local chemical environments, XPS analysis. Fig. S3 (SI) presents the XPS survey spectra for each experimental condition, highlighting the presence of all major constituent elements of the films (Li 1s, O 1s, P 2p, N 1s, and C 1s). To investigate the

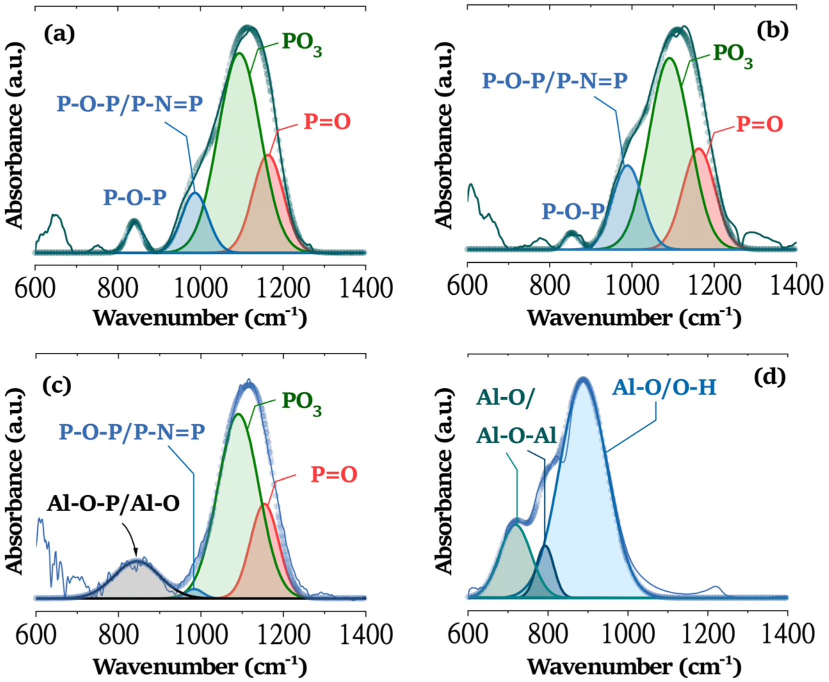

Fig. 6 ATR-FTIR spectra of LiPON, LiPON doped films and Al_2O_3 concentrations: (a) LiPON, (b) $LiAlPON_{(10:1)}$ (c) $LiAlPON_{(1:1)}$ (d) Al_2O_3.

effects of Al_2O_3 insertion in LiPON, the binding environments of each element were systematically monitored and presented as a function of doping ratio in Fig. 7.

The presence of Al dopants in LiPON, introduced through TMA–H_2O pulses, was confirmed by the Al 2p spectrum shown in Fig. S4 (SI). At doping ratios of 1 : 20 and 1 : 10, the Al 2p signal was only marginally detected at 73.6 eV (±0.1 eV), whereas at a 1 : 1 ratio the peak became significantly more intense, indicating an excess of Al_2O_3 within the LiPON. The Al 2p peak in the doped LiPON films is slightly shifted toward lower binding energy upon doping. This shift may indicate a modification of the Al chemical environment relative to Al_2O_3, consistent with the formation of Al-phosphate/oxide bonding environments within the doped LiPON matrix.[31]

From the C 1s spectrum in Fig. S5 (SI), the peaks at 285, 286, 287.5, and 290 eV are assigned to C–C/C–H, C–O, C=O, and CO_3^{2-}, respectively.[51] The C–C/C–H components mainly originate from precursor by-products and atmospheric impurities,[22] while the CO_3^{2-} peak indicates the formation of lithium carbonate (Li_2CO_3) on the film surface.[22] Upon Al_2O_3 incorporation, a decrease in C–C/C–H content is observed, potentially due to the increased H_2O pulse that facilitates removal of the carbon fragments.[21,52] However, an excessive H_2O exposure may also enhance surface reactivity, promoting lithium carbonate formation,[53] which is particularly noticed at the highest doping ratio.

The Li 1s spectra are symmetrical, positioned around a binding energy of 55.3 eV (±0.1 eV) and composed of a unique singlet[24] with minor variations in shape and binding energy upon doping. The P 2p peaks are constituted of two spin–orbit components closely spaced by 0.9 eV.[17] The P $2p_{3/2}$ component is located around 132.7 eV (±0.1 eV), while the P $2p_{1/2}$ component is around 133.6 eV (±0.1 eV) and the binding energies of the two components seem to be practically unchanged with

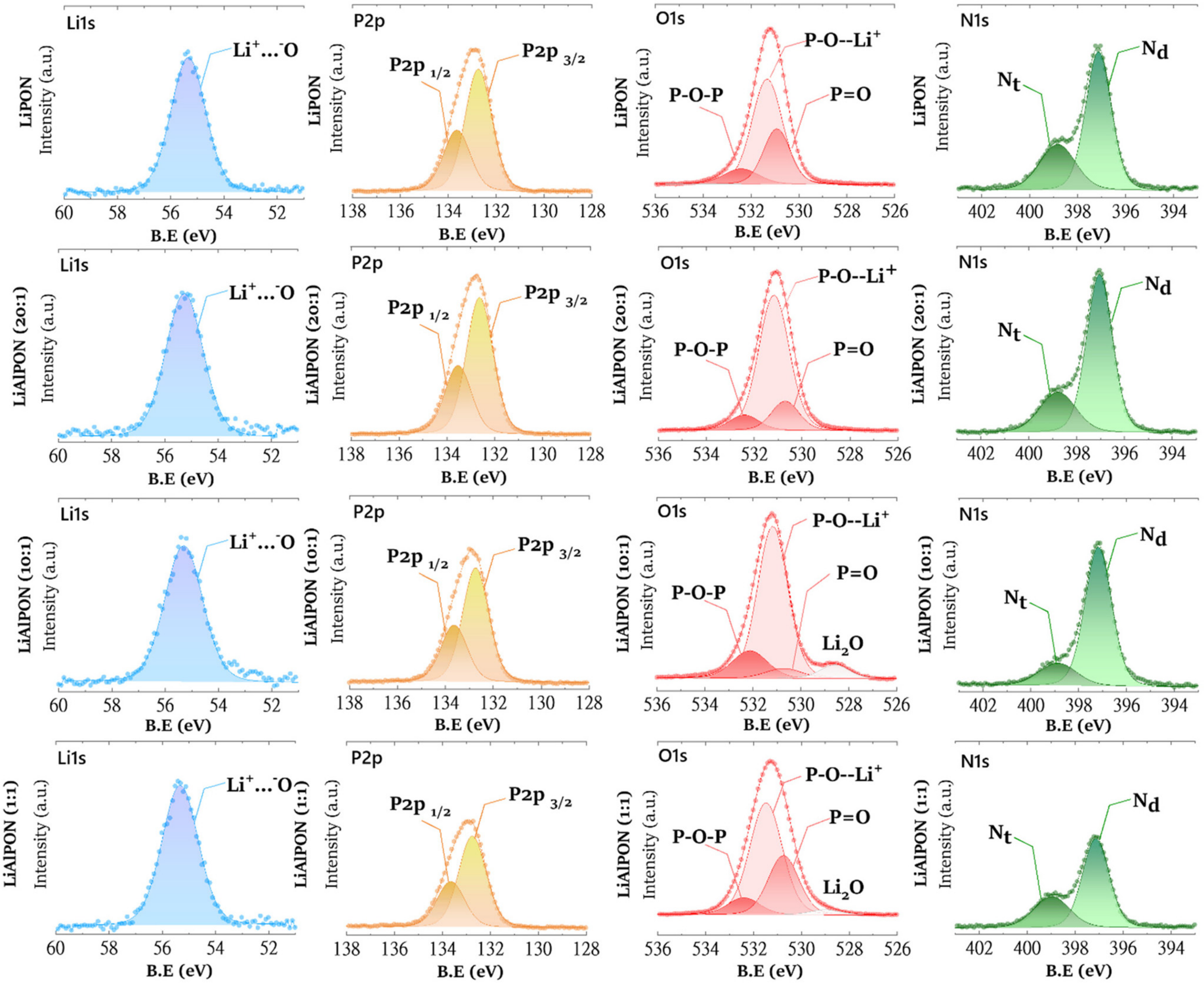

Fig. 7 High-resolution core-level XPS spectra (columns) of LiPON and LiAlPON doped films (dotted lines correspond to the measured spectra and solid lines to the fitted envelop. Coloured lines refer to the assigned environments).

doping. The first (P $2p_{3/2}$) corresponds to PO_4^{3-} phosphate groups, similar to those present in Li_3PO_4,[17] while the second component (P $2p_{1/2}$) is attributed to cross-linking environments such as P–O–N and P–O–P within the amorphous LiPON network.[24]

While the phosphorus and lithium environment seemed to be non-influenced by Al_2O_3 insertion, O 1s and N 1s exhibited some variations. Based on the previous studies on alkali phosphate glasses,[17] the O 1s core peak can be deconvoluted into four main environments composed of oxide species (Li_2O) at 528.5 eV (±0.1 eV), non-bridging oxygen(II) ($NBO_{(II)}$) (P=O) at 530.1 eV, non-bridging oxygen(I) ($NBO_{(I)}$) ($P–O^-\cdots Li^+$) at 531.2 eV (±0.1 eV) and bridging oxygen (BO) (P–O–P) at 532.5 eV (±0.1 eV).

This BO peak can also be related to X–O–P moieties (such as X = Al, Si, C),[17,35,54,55] suggesting that aluminum has been effectively incorporated into LiPON in the form of Al–O–P sequences which is consistent with our FTIR data, in which the P–O–P/P=N–P peak (950–1000 cm^{-1}) increased for $LiAlPON_{(10:1)}$ configuration compared to pure LiPON. The insertion of aluminum ions is expected to effectively improve the cross-linkage between phosphate groups by creating silica-like structural units, where $NBO_{(II)}$ (P=O) bonds tend to be progressively substituted by Al–O–P bonds.[35,56] In the O 1s spectra, we indeed observe a gradual decrease of the peak intensity of $NBO_{(II)}$ accompanied by an increase in the BO contribution, supporting the substitution of P=O groups by newly formed Al–O–P linkages. A similar trend has been reported on silicon-doped LiPON films, where Si has replaced phosphorus, resulting in a higher cross-linkage density by the prevalence of (Si–O–P) bonds over P=O.[17] The N 1s spectra highlight two distinct chemical environments at approximately 397 eV (±0.1 eV) and 399 eV (±0.1 eV), generally assigned to divalent nitrogen (N_d) and trivalent nitrogen (N_t) states, respectively.[17] Similarly to the O 1s spectra, the insertion of Al_2O_3 has induced a rearrangement in the nitrogen environment. Notably, the divalent nitrogen peak has become predominant over the trivalent nitrogen peak, leading to an increased N_d/N_t ratio (Fig. 8).

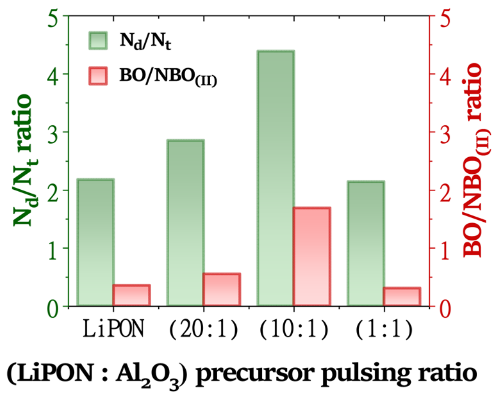

Fig. 8 N_d/N_t and $BO/NBO_{(II)}$ ratios extracted from XPS data for LiAlPON films with varying Al_2O_3 content.

It is commonly assumed that the coexistence of N_d and N_t in the LiPON matrix is primarily influenced by the originating distribution of oxygen, specifically (NBO) and (BO).[57] R. Marchand *et al.* have explored these synergistic variations between oxygen and nitrogen environments.[57] Their studies denote that an increase in N_d (–N=P) groups can be coupled with the breaking of $NBO_{(II)}$ (P=O) groups. Comparable trends have been observed in the study of V. Torres *et al.*,[58] where the presence of N_t promoted the formation of more $NBO_{(II)}$ sites. In our case, considering phosphorus as a pentavalent element within PO_3N units, we can reasonably suggest that loss of P=O bond is simultaneously compensated by generating new –N=P bonds resulting in a rise of the N_d/N_t ratio.

By further increasing the alumina concentration $LiAlPON_{(1:1)}$, beyond the optimal doping ratio of 10 : 1, the positive trend of N_d/N_t and $BO/NBO_{(II)}$ ratios is inverted leading to lower values. This transition reasonably originates from the excess of aluminum atoms in the local structure, potentially disrupting LiPON network. This finding is supported by FTIR analysis of $LiAlPON_{(1:1)}$ configuration which displayed significant decrease in P–O–P/P=N–P peak intensity.

Elemental composition, XPS analysis. The binding energies and atomic concentrations (at.%) of the different chemical environments identified by XPS are reported in Table S1 (SI). To gain further insight, Table 2 summarizes the LiPON composition variations upon Al_2O_3 incorporation.

When increasing the insertion of Al_2O_3, a gradual rise in aluminum and oxygen content was observed, denoting that the injected ($TMA–H_2O$) monocycle successfully generated trace doping amounts of Al_2O_3 and possibly intrinsic rearrangements during film growth.[35,35,59] Accordingly, a par-

Table 2 The chemical composition obtained from XPS quantitative analysis for LiPON and LiPON Al-doped films

	Atomic composition (%)						
Films	Li	P	O	N	Al	C	Composition[a]
LiPON	27.1	12.2	34.5	13.1	0	12.3	$Li_{2.2}PO_{2.7}N$
$LiAlPON_{(20:1)}$	28.9	12.6	34.6	13.1	0.3	9.6	$Li_{2.3}\,(Al_{0.02})\,PO_{2.7}N$
$LiAlPON_{(10:1)}$	31.3	11.5	35.1	12	0.6	8.4	$Li_{2.7}\,(Al_{0.05})\,PO_3N$
$LiAlPON_{(1:1)}$	24.1	8.9	40.7	8.6	2.7	8.3	$Li_{2.7}\,(Al_{0.3})\,PO_{4.5}N$

[a] Composition relative to P excluding C.

allel decrease in phosphorus and nitrogen concentrations was noticed, suggesting a potential substitution of phosphorus by aluminium and the formation of new Al–O–P sequences. The overall carbon content has decreased upon doping, due to the removal of precursors by-products during the H_2O pulses.[21,52]

For lithium content, it displayed an increase as a function of Al_2O_3 insertion, evolving from LiPON to $LiAlPON_{(10:1)}$. Accordingly, M. J. Pieters *et al.*[60] have reported that LiHMDS favorably chemisorb on hydroxyl groups (–OH). Thus, we expect that injecting water molecules during Al_2O_3 insertion, would provide superior concentration of OH-active sites on the surface, enabling an improved chemisorption of LiHMDS molecules and resulting in enhanced lithium content.

However, at the highest doping ratio ($LiAlPON_{(1:1)}$), a significant increase in aluminum and oxygen concentrations was observed, accompanied by a drop in phosphorus, nitrogen, and lithium contents. This is likely due to the formation of a larger Al-phosphate/oxide bonding environments within the doped LiPON matrix. This is evidenced by the intense peak at 73.5 eV in the Al 2p spectrum in Fig. S4 (SI). This outcome could suggest that LiPON structure begins to be altered at higher Al_2O_3 incorporation.

3.3. Electrochemical investigation

Ionic conductivity, EIS analysis. The ionic conductivity at room temperature was measured for pure LiPON films and its doped homologues using electrochemical impedance spectroscopy (EIS). From Fig. 9(a), the resulting Nyquist plots display a semicircle in the high-frequency region and a straight line at low-frequency region. The semicircle is associated with the resistive properties of the solid state electrolyte, while the sloped line is attributed to the blocking electrode, displays the polarization at the electrode–electrolyte interface,[61] which is typical of thin film ionic conductors.

The EIS spectra were fitted with an equivalent circuit shown in Fig. S6(c) (SI). The ionic conductivity (σ_i) is calculated based on the following formula[61]:

$$\sigma_i = d/(R_{\text{bulk}} \times A)$$

where d is the film thickness, R_{bulk} is the electrolyte resistance and A is the electrode's geometric area.

To study the interplay between the film's composition and ionic mobility, all samples were prepared with a thickness of 30 nm. The incorporation of aluminum atoms within LiPON structure induced a gradual decrease in the film resistance leading to a progress in ionic conductivities. Hence, for pure LiPON and the optimally doped $LiAlPON_{(10:1)}$ films, the measured ionic conductivities at 25 °C, were 1.8×10^{-8} S cm^{-1} and 8.8×10^{-8} S cm^{-1} respectively. This increase aligns well with XPS data showing a rise of N_d/N_t and $BO/NBO_{(II)}$ ratios as well as an enrichment in lithium content and a decrease in carbon content upon Al_2O_3 incorporation. This suggests that ionic conductivity might be closely linked to lithium and carbon concentrations, along with the local nitrogen and oxygen bonding.

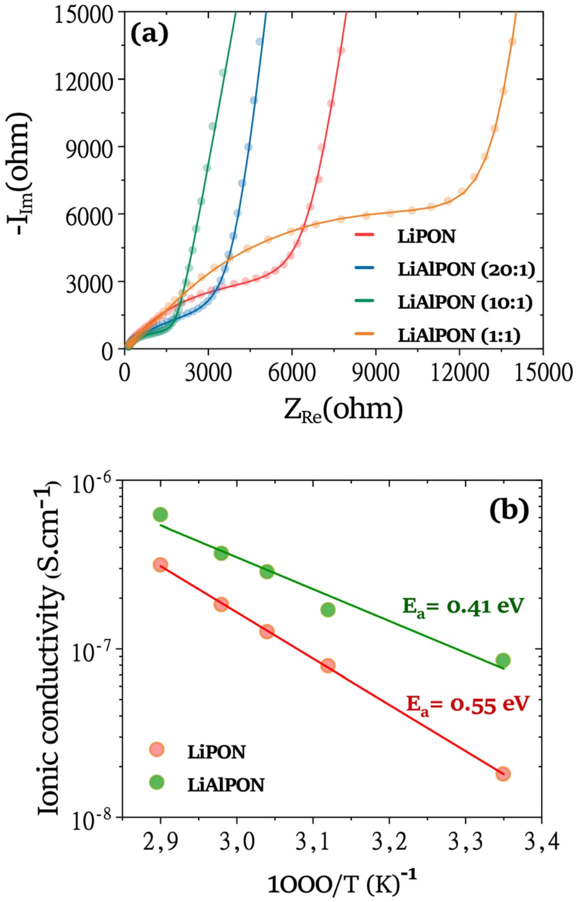

Fig. 9 (a) Nyquist impedance plots of LiPON and $LiAlPON_{(1:10)}$ films at different doping concentrations at 25 °C (Solid lines correspond to the fitted curve and dots to the measured spectra). (b) Arrhenius plot of ionic conductivity *versus* 1000/*T* of LiPON and $LiAlPON_{(1:10)}$.

The increase of bridging oxygen (P–O–P and Al–O–P) concentration is intended to enhance the cross-linking within the LiPON matrix, thereby contributing to improved ionic conductivity.[17] Upon doping, the formation of (BO) sequences appeared to be at the expense of $NBO_{(II)}$ sequences. These non-bridging oxygens are known to hinder Li^+ mobility due to their localized negative charge.[53,60,62] Hence their decrease would further facilitate the lithium-ion transport.

From nitrogen side, studies by A. K. Landry *et al.*,[63] denoted that trivalent nitrogen (N_t) does not significantly contribute to Li^+ transport mechanisms and their presence may reflect an unstable nature of LiPON surface. Therefore, the gradual predominance of N_d over N_t species upon doping can also have additional influence, supporting the ionic conductivity. Accordingly, studies by V. Lacivita *et al.*[64] highlighted that divalent nitrogen (N_d) can effectively reduce electrostatic interactions, thereby stimulating Li^+ ion mobility.

Furthermore, the increase in lithium content is intended to enhance the number of mobile Li^+ charge carriers available for transport,[64] contributing to higher ionic conductivity. In parallel, the lower carbon content can also reflect the limited presence of carbonaceous species in the bulk, promoting a cleaner LiPON network.

When alumina concentration exceeds the optimal doping ratio of (10 : 1), the ionic conductivity has significantly diminished to approximately 1.42×10^{-8} S cm^{-1}. This drop of ionic conductivity after the optimum coincides with a rise of N_d/N_t and BO/NBO$_{(II)}$ ratios, as well as an increase in carbonate content, which is indicative of reversible local structural alterations, potentially leading to enhanced electrostatic interactions with Li$^+$ ions.[53]

Before delving into further comparative trends, it should be noted that the measured ionic conductivity was unexpectedly lower than usual values of LiPON films.[21] This discrepancy mainly originates from the formation of residual resistive interphases (*i.e.* Lithium carbonate species) induced by air exposure of LiPON prior to MIM fabrication and during electrochemical measurements.[65,66] Such interphases have been reported to attenuate LiPON's ionic conductivity (~2×10^{-8} S cm^{-1}).[66] LiPON thin films are known to degrade rapidly in ambient air,[22,53,67] and although considerable attention was given to minimizing exposure, the formation of a metastable surface cannot be completely excluded,[22] potentially contributing to additional interfacial impedance. Nevertheless, the primary goal anticipated from Al_2O_3 doping effect is preserved and clearly evidenced by the progress in ionic conductivity, the concurrent reduction of activation energy and the structural rearrangements. Hence, an optimization of surface protection and the use of an argon atmosphere during analysis, are expected to yield higher ionic performance,[65] for both pristine and Al_2O_3-doped LiPON films.

Activation energies. Temperature-dependent EIS measurements (Fig. S6(a) and (b) (SI)) were conducted to assess the activation energy of Li$^+$ transport in the films. Fig. 9(b) exhibits a gradual increase in ionic conductivities as temperature rises, reaching 3.1×10^{-7} S cm^{-1} and 6.2×10^{-7} S cm^{-1} at ~75 °C for LiPON and LiAlPON$_{(10:1)}$ respectively. Thus, activation energies (E_a) of both electrolytes were evaluated based on the linearized Arrhenius equation:[63]

$$\sigma T = \sigma_0 e^{-(E_a/k_B T)}$$

where (k_B) is the Boltzmann constant, (σ_0) is the pre-exponential factor, (E_a) is the activation energy and (T) is the absolute temperature. Hence, (E_a) is extracted from the fitted slope of the linear curves ($\log(\sigma)$ *vs.* $1000/T$). The values indicate an activation energy value of 0.55 eV for LiPON, which is within the expected range as previously reported for LiPON films (from 0.5 to 0.6 eV),[22,65,68] suggesting that when thermally activated, LiPON can exhibit the usual ion-transport characteristics. When Al_2O_3 is incorporated, the slope has diminished, leading to a lower activation energy of 0.41 eV. This indicates that the Al-induced structural rearrangements reduce the energy barrier for ion motion, thereby facilitating Li$^+$ migration.[67,69]

Characteristic frequencies. In Fig. 10, we observe the evolution of the imaginary part of the capacitance. The curves took on a characteristic bell-shapes, with a characteristic frequency identified at the peak of the curves. These maximum values reflect the transition between the capacitive and resistive behavior of the microsupercapacitor, and are used to calculate the relaxation time (τ), which refers to the duration required to charge/discharge the MSC.[70,71] In standard MSC systems, the relaxation time is generally influenced by the Li$^+$ mobility within the electrolyte layer, leading to a reduced charge/discharge duration due to elevated ionic conductivity.[61]

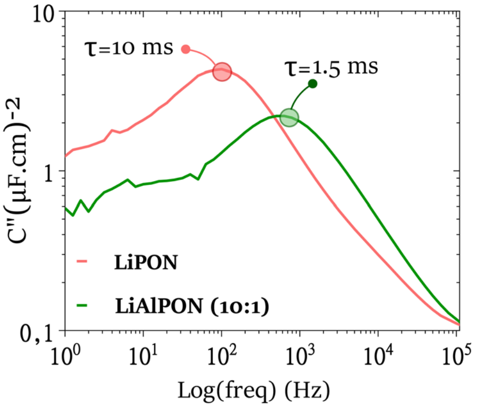

Fig. 10 Frequency dependence of the imaginary part of the capacitance of LiPON and LiAlPON$_{(10:1)}$ at 25 °C.

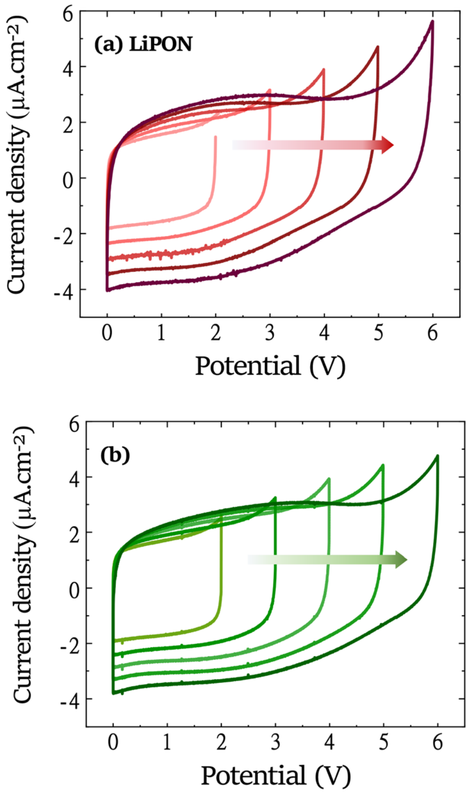

Fig. 11 Cyclic voltammograms of (a) LiPON and (b) LiAlPON$_{(10:1)}$ doped thin films in the voltage range of 0–6 V at the scan rate of 100 mV s^{-1}.

Accordingly, at 25 °C, the characteristic frequency for LiPON is f_{LiPON} = 100 Hz, while with doping ($\text{LiAlPON}_{(10:1)}$), it increases to f_{LiAlPON} = 631 Hz. This increase in cut-off frequency results in a corresponding decrease in the relaxation time constant (calculated as $1/f$), which shifts from τ_{LiPON} = 10 ms to τ_{LiAlPON} = 1.5 ms at 25 °C. These improvements are in agreement with previous reports for thermally activated LiPON, which exhibited relaxation times ranging from 1 to 5 ms at 35 °C.[13]

Electrochemical stability window. To assess the potential window stability and evaluate the existence of redox processes between LiPON-based films and electrodes,[72,73] cyclic voltammetry was performed over the 0–6 V range, at a scan rate of 100 mV s^{-1}. Fig. 11(a) shows that the pure LiPON film exhibits a stable electrochemical response across a wide potential window, with a quasi-ideal double-layer behaviour.[61] Additionally, the structural rearrangements from doping may plausibly influence the voltammogram response or the electrochemical stability of LiPON.[15,74] Nevertheless, the quasi-rectangular CV shape remains well preserved after incorporating Al into the film (Fig. 11(b)), with no noticeable cathodic or anodic peaks even at elevated voltages. This indicates that the Al insertion does not hinder the highly reversible charge–discharge processes and effectively preserves a wide potential-window stability. At 6 V, a rise in current density is noticed at the high voltage boundary, which may indicate the beginning of a redox activity.[13]

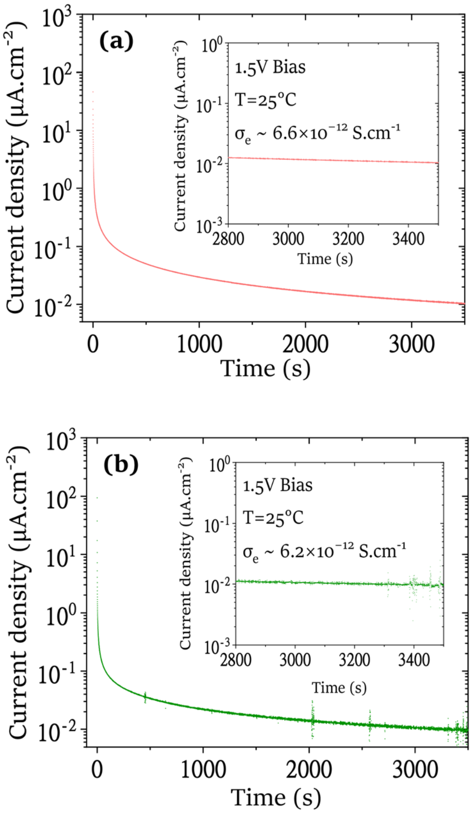

Fig. 12 DC polarization curves of (a) LiPON and (b) $\text{LiAlPON}_{(10:1)}$ doped thin films under a 1.5 V polarization voltage.

The electrochemical stability window of conventional LiPON is generally reported to reach values of around 5.5 V.[15,16] To further examine possible degradation effects, CV measurements were extended to higher voltages (>6 V) (Fig. S7 (SI)). As expected, both films exhibited signs of alteration near 7 V, which can be attributed to electrolyte decomposition.[61]

Electronic leakage analysis. We carried out chronoamperometry to determine the DC leakage current, as shown in Fig. 12(a) and (b). A DC voltage of 1.5 V was applied and the current density was monitored over time. The *J*–*t* responses exhibit the typical relaxation behavior for a LiPON-based capacitor.[66] The leakage current was then extracted from the average value of the plateau during the final stage of the measurement.[17]

Slight fluctuations were observed in the response of the doped LiPON film. These minor noise (as illustrated in the inset of Fig. 12(b)) may originate from the modified structure of LiPON.[13] However, the steady-state current density section of $\text{LiAlPON}_{(10:1)}$ remains well below 0.1 μA cm^{-2}, showing the expected insulating property of the film.[16,24] The corresponding electronic conductivities of the films were determined, yielding values of $\sigma_e \approx (6.2\text{–}6.6) \times 10^{-12}$ S cm^{-1}, which is in agreement with ALD-LiPON studies.[22,25] The electronic conductivity is approximately four orders of magnitude lower than the Li^+ ionic conductivity values, indicating that the films behave predominantly as ionic conductors.[70]

4. Conclusion

In this work, we explored the potential of atomic layer deposition to rearrange the structure of LiPON thin films (<50 nm). A multidisciplinary study was conducted to generate and investigate LiAlPON films as solid-state electrolytes for microsupercapacitor applications. An ALD super-cycle method was implemented to modulate Al_2O_3 concentrations and fine-tune film growth during the doping process. The resulting amorphous films demonstrated good conformality on the 3D structures, making them a promising candidate for next-generation device architectures. Using TOF-SIMS depth profiling, we demonstrated a homogeneous distribution of aluminum throughout the bulk underlining the efficiency of the supercycle approach. Furthermore, FTIR and XPS analysis enabled us to relate Li^+ conductivity trends and showed that multiple factors can contribute to the improved performance of doped-LiPON including: (i) the enrichment in lithium(II) the reduced carbon content (iii) the increase in the bridging oxygen (BO) to non-bridging oxygen (NBO) ratio (iiii) and the higher prevalence of divalent nitrogen (N_d) units. These structural rearrangements are intended to enhance the network cross-linking while reducing the electrostatic confinement effect on Li^+ ions, thereby improving their mobility. We then demonstrated the elevation of ionic conductivity upon LiPON doping, with unexpectedly attenuated values. This weakening mainly originates from the high surface sensitivity of LiPON before and during analysis, particularly at such reduced thicknesses

(<50 nm). These findings have opened a new perspective for future studies aimed at exploring degradation mechanisms of LiPON-ALD under air exposure. Nevertheless, the beneficial effect of Al_2O_3 incorporation is maintained, leading to a lower activation energy (0.41 eV) compared to pristine LiPON (0.55 eV), faster charge/discharge response and maintaining a wide electrochemical stability window.

Although this study is primarily focused on LiPON electrolyte, from a more general viewpoint, it provides an initial step toward transitioning LiPON doping, from PVD to ALD configuration, while also opening new pathways for enhancing several ALD-grown ion-conducting polyphosphazenes (*i.e.*, NaPON, KPON).

Author contributions

Ghandari Ilyass: conceptualization, manuscript writing, data curation, process development, investigation, formal analysis, validation. Gauthier Nicolas: review & editing, investigation, validation. Rochat Névine: investigation, review & validation. Casiez Lara: review & investigation. Poulet Sylvain: process development & investigation. Letiche Manon: review & validation. Hélène Coudert-Alteirac: ellipsometry experimentation, Vaxelaire Nicolas: XRD experimentation. Salvador Violaine: SEM imaging. Bechelany Mikhael: review & editing, validation. Bedjaoui Messaoud: conceptualization, formal analysis, visualization, review, validation.

Conflicts of interest

The authors declare no competing financial interest.

Data availability

All data supporting the findings of this study are available within the article and its supplementary information (SI). Supplementary information is available. See DOI: https://doi.org/10.1039/d5dt02597d.

Acknowledgements

Part of this work, carried out on the Platform for Nanocharacterisation (PFNC), was supported by the 'Recherches Technologiques de Base' program.

References

1 K. O. Oyedotun and B. B. Mamba, New Trends in Supercapacitors Applications, *Inorg. Chem. Commun.*, 2024, **170**, 113154, DOI: 10.1016/j.inoche.2024.113154.

2 J. Son, H. Kim, Y. Choi and H. Lee, 3D Printed Energy Devices: Generation, Conversion, and Storage, *Microsyst. Nanoeng.*, 2024, **10**(1), 93, DOI: 10.1038/s41378-024-00708-2.

3 Q. Muhammad Saqib, A. Mannan, M. Noman, M. Y. Chougale, C. S. Patil, Y. Ko, J. Kim, S. R. Patil, M. Yousuf, R. Ali Shaukat, Y. Pyo Jeon, D. Dubal and J. Bae, Miniaturizing Power: Harnessing Micro-Supercapacitors for Advanced Micro-Electronics, *Chem. Eng. J.*, 2024, **490**, 151857, DOI: 10.1016/j.cej.2024.151857.

4 B. Chen, Z. T. Johnson, D. Sanborn, R. G. Hjort, N. T. Garland, R. R. A. Soares, B. Van Belle, N. Jared, J. Li, D. Jing, E. A. Smith, C. L. Gomes and J. C. Claussen, Tuning the Structure, Conductivity, and Wettability of Laser-Induced Graphene for Multiplexed Open Microfluidic Environmental Biosensing and Energy Storage Devices, *ACS Nano*, 2022, **16**(1), 15–28, DOI: 10.1021/acsnano.1c04197.

5 K. Calautit, D. S. N. M. Nasir and B. R. Hughes, Low Power Energy Harvesting Systems: State of the Art and Future Challenges, *Renewable Sustainable Energy Rev.*, 2021, **147**, 111230, DOI: 10.1016/j.rser.2021.111230.

6 A. Kumar, Y. Roy, N. Ramachandran, T. Assiri, M. A. Srinivasa Rao, S. Moniruzzaman, M. Joo and S. W, Revolutionizing Energy Storage: Exploring the Nanoscale Frontier of All-Solid-State Batteries, *Dalton Trans.*, 2024, **53**(30), 12410–12433, DOI: 10.1039/D4DT01133C.

7 H. Rashid Khan and A. Latif Ahmad, Supercapacitors: Overcoming Current Limitations and Charting the Course for next-Generation Energy Storage, *J. Ind. Eng. Chem.*, 2025, **141**, 46–66, DOI: 10.1016/j.jiec.2024.07.014.

8 Z. Gao, H. Sun, L. Fu, F. Ye, Y. Zhang, W. Luo and Y. Huang, *Adv. Mater.*, 2018, **30**, 1705702, DOI: 10.1002/adma.201705702.

9 J. Liang, J. Luo, Q. Sun, X. Yang, R. Li and X. Sun, Recent Progress on Solid-State Hybrid Electrolytes for Solid-State Lithium Batteries, *Energy Storage Mater.*, 2019, **21**, 308–334, DOI: 10.1016/j.ensm.2019.06.021.

10 Y. Li, S. Xiao, T. Qiu, X. Lang, H. Tan, Y. Wang and Y. Li, Recent Advances on Energy Storage Microdevices: From Materials to Configurations, *Energy Storage Mater.*, 2022, **45**, 741–767, DOI: 10.1016/j.ensm.2021.12.026.

11 Z. Zou, Z. Xiao, Z. Lin, B. Zhang, C. Zhang and F. Wei, Lithium Phosphorous Oxynitride as an Advanced Solid-State Electrolyte to Boost High-Energy Lithium Metal Battery, *Adv. Funct. Mater.*, 2024, **34**, 2409330, DOI: 10.1002/adfm.202409330.

12 X. Miao, H. Wang, R. Sun, C. Wang, Z. Zhang, Z. Li and L. Yin, Interface Engineering of Inorganic Solid-State Electrolytes for High-Performance Lithium Metal Batteries, *Energy Environ. Sci.*, 2020, **13**(11), 3780–3822, DOI: 10.1039/D0EE01435D.

13 K. Ahuja, V. Sallaz, R. B. Nuwayhid, F. Voiron, P. McCluskey, G. W. Rubloff and K. E. Gregorczyk, Ultra-Thin on-Chip ALD LiPON Capacitors for High Frequency Application, *J. Power Sources*, 2023, **575**, 233056, DOI: 10.1016/j.jpowsour.2023.233056.

14 N. Kuganathan and A. Chroneos, Defects, Dopants and Lithium Incorporation in LiPON Electrolyte, *Comput.*

Mater. Sci., 2022, **202**, 111000, DOI: 10.1016/j.commatsci.2021.111000.

15 W. Huang, J. Li, K. Wei and L. Wang, Boosted Li+ Migration in LiPON Electrolyte via Introducing Ti-Based Bridge for Solid-State Thin Film Batteries, *J. Power Sources*, 2023, **587**, 233698, DOI: 10.1016/j.jpowsour.2023.233698.

16 S. Zhou, R. Tian, A. Wu, L. Lin and H. Huang, Fast Li+ Migration in LiPON Electrolytes Doped by Multi-Valent Fe Ions, *J. Energy Chem.*, 2022, **75**, 349–359, DOI: 10.1016/j.jechem.2022.08.044.

17 Y. Su, J. Falgenhauer, T. Leichtweiß, M. Geiß, C. Lupó, A. Polity, S. Zhou, J. Obel, D. Schlettwein, J. Janek and B. K. Meyer, Electrochemical Properties and Optical Transmission of High Li $^+$ Conducting LiSiPON Electrolyte Films, *Phys. Status Solidi B*, 2017, **254**(2), 1600088, DOI: 10.1002/pssb.201600088.

18 S. Jesse, A. Y. Borisevich, J. D. Fowlkes, A. R. Lupini, P. D. Rack, R. R. Unocic, B. G. Sumpter, S. V. Kalinin, A. Belianinov and O. S. Ovchinnikova, Directing Matter: Toward Atomic-Scale 3D Nanofabrication, *ACS Nano*, 2016, **10**(6), 5600–5618, DOI: 10.1021/acsnano.6b02489.

19 Y. Zhao, L. Zhang, J. Liu, K. Adair, F. Zhao, Y. Sun, T. Wu, X. Bi, K. Amine, J. Lu and X. Sun, Atomic/Molecular Layer Deposition for Energy Storage and Conversion, *Chem. Soc. Rev.*, 2021, **50**(6), 3889–3956, DOI: 10.1039/D0CS00156B.

20 M. Z. Ansari, I. Hussain, D. Mohapatra, S. A. Ansari, R. Rahighi, D. K. Nandi, W. Song and S. Kim, Atomic Layer Deposition—A Versatile Toolbox for Designing/Engineering Electrodes for Advanced Supercapacitors, *Adv. Sci.*, 2024, **11**(1), 2303055, DOI: 10.1002/advs.202303055.

21 A. C. Kozen, A. J. Pearse, C.-F. Lin, M. Noked and G. W. Rubloff, Atomic Layer Deposition of the Solid Electrolyte LiPON, *Chem. Mater.*, 2015, **27**(15), 5324–5331, DOI: 10.1021/acs.chemmater.5b01654.

22 M. Nisula, Y. Shindo, H. Koga and M. Karppinen, Atomic Layer Deposition of Lithium Phosphorus Oxynitride, *Chem. Mater.*, 2015, **27**(20), 6987–6993, DOI: 10.1021/acs.chemmater.5b02199.

23 M. Madadi, M. Heikkinen, A. Philip and M. Karppinen, Conformal High-Aspect-Ratio Solid Electrolyte Thin Films for Li-Ion Batteries by Atomic Layer Deposition, *ACS Appl. Electron. Mater.*, 2024, **6**(3), 1574–1580, DOI: 10.1021/acsaelm.3c01565.

24 V. Sallaz, M. Bedjaoui, S. Poulet, N. Gauthier, S. Prabhakaran, E. Perez, V. Salvador, G. Pillonnet, F. Voiron and S. Oukassi, Dual Storage Mechanism in Nanoscale Solid-State Lithium-Ion Supercapacitors, *ACS Electrochem.*, 2024, DOI: 10.1021/acselectrochem.4c00022.

25 T. Tsuruoka, S. Mallik, T. Tsujita, Y. Inatomi and K. Terabe, Effects of Plasma Reactants on Atomic Layer Deposition of Lithium Phosphate and Lithium Phosphorus Oxynitride Electrolyte Films, *Chem. Mater.*, 2024, **36**(12), 6193–6204, DOI: 10.1021/acs.chemmater.4c00960.

26 G. Tan, F. Wu, L. Li, Y. Liu and R. Chen, Magnetron Sputtering Preparation of Nitrogen-Incorporated Lithium–Aluminum–Titanium Phosphate Based Thin Film Electrolytes for All-Solid-State Lithium Ion Batteries, *J. Phys. Chem. C*, 2012, **116**(5), 3817–3826, DOI: 10.1021/jp207120s.

27 E. Quartarone and P. Mustarelli, Electrolytes for Solid-State Lithium Rechargeable Batteries: Recent Advances and Perspectives, *Chem. Soc. Rev.*, 2011, **40**(5), 2525, DOI: 10.1039/c0cs00081g.

28 A. Patil, V. Patil, D. Wook Shin, J. W. Choi, D.-S. Paik and S.-J. Yoon, Issue and Challenges Facing Rechargeable Thin Film Lithium Batteries, *Mater. Res. Bull.*, 2008, **43**(8–9), 1913–1942, DOI: 10.1016/j.materresbull.2007.08.031.

29 M. L. Xie, X. Lin, Z. M. Huang, Y. Y. Li, Y. Zhong, Z. X. Cheng, L. X. Yuan, Y. Shen, X. Lu, T. Y. Zhai and Y. H. Huang, A Li–Al–O Solid-State Electrolyte with High Ionic Conductivity and Good Capability to Protect Li Anode, *Adv. Funct. Mater.*, 2020, **30**, 1905949, DOI: 10.1002/adfm.201905949.

30 J. Li, M. Jing, R. Li, L. Li, Z. Huang, H. Yang, M. Liu, S. Hussain, J. Xiang and X. Shen, Al_2 O_3 Fiber-Reinforced Polymer Solid Electrolyte Films with Excellent Lithium-Ion Transport Properties for High-Voltage Solid-State Lithium Batteries, *ACS Appl. Polym. Mater.*, 2022, **4**(10), 7144–7151, DOI: 10.1021/acsapm.2c01034.

31 N. Hornsveld, W. M. M. Kessels and M. Creatore, Atomic Layer Deposition of Aluminum Phosphate Using $AlMe_3$, PO $(OMe)_3$, and O_2 Plasma: Film Growth and Surface Reactions, *J. Phys. Chem. C*, 2020, **124**(9), 5495–5505, DOI: 10.1021/acs.jpcc.0c00301.

32 L. Henderick, H. Hamed, F. Mattelaer, M. Minjauw, J. Meersschaut, J. Dendooven, M. Safari, P. Vereecken and C. Detavernier, Atomic Layer Deposition of Nitrogen-Doped Al Phosphate Coatings for Li-Ion Battery Applications, *ACS Appl. Mater. Interfaces*, 2020, **12**(23), 25949–25960, DOI: 10.1021/acsami.0c05585.

33 Z. Feng, Y. Wang, J. Hao, M. Jing, F. Lu, W. Wang, Y. Cheng, S. Wang, H. Liu and H. Dong, Designing High *k* Dielectric Films with LiPON—Al_2O_3 Hybrid Structure by Atomic Layer Deposition, *Chin. Phys. B*, 2022, **31**(5), 057701, DOI: 10.1088/1674-1056/ac3736.

34 E. Schilirò, P. Fiorenza, G. Greco, F. Monforte, G. G. Condorelli, F. Roccaforte, F. Giannazzo and R. Lo Nigro, Early, Growth Stages of Aluminum Oxide (Al_2O_3) Insulating Layers by Thermal- and Plasma-Enhanced Atomic Layer Deposition on AlGaN/GaN Heterostructures, *ACS Appl. Electron. Mater.*, 2022, **4**(1), 406–415, DOI: 10.1021/acsaelm.1c01059.

35 S. K. Barik, A. Senapati, S. Balakrishnan and K. Ananthasivan, Synthesis and Characterization of Rare-Earth Doped Aluminium Phosphate Glasses, *Prog. Nucl. Energy*, 2022, **152**, 104372, DOI: 10.1016/j.pnucene.2022.104372.

36 S. Ng, C. Iffelsberger, J. Michalička and M. Pumera, Atomic Layer Deposition of Electrocatalytic Insulator Al_2 O_3 on Three-Dimensional Printed Nanocarbons, *ACS Nano*, 2021, **15**(1), 686–697, DOI: 10.1021/acsnano.0c06961.

37 Y. Kim, K. Kim, O. Kim, C. Y. Park, D. G. Koo, D.-H. Ahn, B. J. Kuh and W.-J. Lee, Composition Control of Conformal Crystalline GeSbTe Films by Atomic Layer Deposition

Supercycles and Tellurization Annealing, *J. Mater. Chem. C*, 2022, **10**(1), 9691–9698, DOI: 10.1039/D2TC00784C.

38 J. G. Baker, J. R. Schneider, J. A. Raiford, C. de Paula and S. F. Bent, Nucleation Effects in the Atomic Layer Deposition of Nickel–Aluminum Oxide Thin Films, *Chem. Mater.*, 2020, **32**(5), 1925–1936, DOI: 10.1021/acs.chemmater.9b04630.

39 D. Nazarov, L. Kozlova, A. Rudakova, E. Zemtsova, N. Yudintceva, E. Ovcharenko, A. Koroleva, I. Kasatkin, L. Kraeva, E. Rogacheva and M. Maximov, Atomic Layer Deposition of Chlorine Containing Titanium–Zinc Oxide Nanofilms Using the Supercycle Approach, *Coatings*, 2023, **13**(5), 960, DOI: 10.3390/coatings13050960.

40 Y. G. Kim and H. N. G. Wadley, Lithium Phosphorous Oxynitride Films Synthesized by a Plasma-Assisted Directed Vapor Deposition Approach, *J. Vac. Sci. Technol., A*, 2008, **26**(1), 174–183, DOI: 10.1116/1.2823491.

41 M. A. Carrillo Solano, M. Dussauze, P. Vinatier, L. Croguennec, E. I. Kamitsos, R. Hausbrand and W. Jaegermann, Phosphate Structure and Lithium Environments in Lithium Phosphorus Oxynitride Amorphous Thin Films, *Ionics*, 2016, **22**(4), 471–481, DOI: 10.1007/s11581-015-1573-1.

42 R. Takakura, S. Murakami, K. Watanabe and R. Takigawa, Room-Temperature Bonding of Al_2O_3 Thin Films Deposited Using Atomic Layer Deposition, *Sci. Rep.*, 2023, **13**(1), 3581, DOI: 10.1038/s41598-023-30376-7.

43 K. Khojier, H. Savaloni, E. Shokrai, Z. Dehghani and N. Dehnavi, Influence of Argon Gas Flow on Mechanical and Electrical Properties of Sputtered Titanium Nitride Thin Films, *J. Theor. Appl. Phys.*, 2013, **7**(1), 37, DOI: 10.1186/2251-7235-7-37.

44 H. T. Kim, T. Mun, C. Park, S. W. Jin and H. Y. Park, Characteristics of Lithium Phosphorous Oxynitride Thin Films Deposited by Metal-Organic Chemical Vapor Deposition Technique, *J. Power Sources*, 2013, **244**, 641–645, DOI: 10.1016/j.jpowsour.2012.12.109.

45 N. Kuwata, N. Iwagami, Y. Tanji, Y. Matsuda and J. Kawamura, Characterization of Thin-Film Lithium Batteries with Stable Thin-Film Li3PO4 Solid Electrolytes Fabricated by ArF Excimer Laser Deposition, *J. Electrochem. Soc.*, 2010, A521.

46 N.-S. Roh, S.-D. Lee and H.-S. Kwon, Effects of Deposition Condition on the Ionic Conductivity and Structure of Amorphous Lithium Phosphorus Oxynitrate Thin Film, *Scr. Mater.*, 1999, **42**(1), 43–49, DOI: 10.1016/s1359-6462(99)00307-3.

47 K. Djebaili, Z. Mekhalif, A. Boumaza and A. Djelloul, XPS, FTIR, EDX, and XRD Analysis of Al_2O_3Scales Grown on PM2000 Alloy, *J. Spectrosc.*, 2015, 1–16, DOI: 10.1155/2015/868109.

48 R. R. Toledo, V. R. Santoyo and D. M. Sánchez, Effect of Aluminum Precursor on Physicochemical Properties of Al_2O_3 by Hydrolysis/Precipitation Method, *Nova Scientia*, 2018, **10**, 83–99.

49 R. Blomme, A. Chalishazar, L. Henderick, F. Munnik, J. Meersschaut, M. M. Minjauw, C. Detavernier and J. Dendooven, Atomic Layer Deposition of Aluminum Phosphate Layers Using Tris(Dimethylamino)Phosphine as P-Precursor, *J. Vac. Sci. Technol., A*, 2025, **43**(2), 022409, DOI: 10.1116/6.0004267.

50 A. M. Saat, A. A. Malik, A. Azmi, M. F. A. Latif, N. Ermadiana and M. R. Johan, Effect of aluminum phosphate on structural and flame retardant properties of composites fibreglass, *ARPN J. Eng. Appl. Sci.*, 2017, **12**(4), 1237–1240.

51 H. Mokudai, T. Takeuchi, H. Sakaebe, H. Kobayashi and E. Matsubara, Degradation Mechanisms of Lithium Sulfide (Li_2 S) Composite Cathode in Carbonate Electrolyte and Improvement by Increasing Electrolyte Concentration, *Sustainable Energy Fuels*, 2021, **5**(6), 1714–1726, DOI: 10.1039/D0SE01112F.

52 M. J. Young, S. Letourneau, R. E. Warburton, W. M. Dose, C. Johnson, J. Greeley and J. W. Elam, Following Carbonate Removal and Formation of Li-Rich Interface by ALD Treatment Carbonate Removal by TMA H_2O, *J. Phys. Chem. C*, 2019, **123**(39), 23783–23790, DOI: 10.1021/acs.jpcc.9b04418.

53 C. S. Nimisha, G. M. Rao, N. Munichandraiah, G. Natarajan and D. C. Cameron, Chemical and Microstructural Modifications in LiPON Thin Films Exposed to Atmospheric Humidity, *Solid State Ionics*, 2011, **185**(1), 47–51, DOI: 10.1016/j.ssi.2011.01.001.

54 C. M. Navarathna, J. E. Pennisson, N. B. Dewage, C. Reid, C. Dotse, M. E. Jazi, P. M. Rodrigo, X. Zhang, E. Farmer, C. Watson, D. O. Craig, A. Ramirez, M. Walker, S. Madduri, D. Mohan and T. E. Mlsna, Adsorption of Phosphates onto Mg/Al-Oxide/Hydroxide/Sulfate-Impregnated Douglas Fir Biochar, *Processes*, 2022, **11**(1), 111, DOI: 10.3390/pr11010111.

55 X. Wu, K. Gong, G. Zhao, W. Lou, X. Wang and W. Liu, Mechanical Synthesis of Chemically Bonded Phosphorus–Graphene Hybrid as High-Temperature Lubricating Oil Additive, *RSC Adv.*, 2018, **8**(9), 4595–4603, DOI: 10.1039/c7ra11691h.

56 B. C. Bunker, G. W. Arnold, M. Rajaram and D. E. Day, Corrosion of Phosphorus Oxynitride Glasses in Water and Humid Air, *J. Am. Ceram. Soc.*, 1987, **70**(6), 425–430, DOI: 10.1111/j.1151-2916.1987.tb05663.x.

57 R. Marchand, D. Agliz, L. Boukbir and A. Quemerais, Characterization of Nitrogen Containing Phosphate Glasses by X-Ray Photoelectron Spectroscopy, *J. Non-Cryst. Solids*, 1988, **103**(1), 35–44, DOI: 10.1016/0022-3093(88)90413-9.

58 V. Torres, S. Kmiec, C. Martin, P. Phillip and S. W. Martin, Impact of LiPON Incorporation on the Ionic Conductivity of Mixed Oxy-Sulfide Glassy Solid Electrolytes, *J. Mater. Chem. A*, 2025, **13**, 27713–27724, DOI: 10.1039/D5TA02481A.

59 A. Werbrouck, F. Mattelaer, A. Dhara, M. Nisula, M. Minjauw, F. Munnik, J. Dendooven and C. Detavernier, Surface Reactions between LiHMDS, TMA and TMP Leading to Deposition of Amorphous Lithium Phosphate,

J. Mater. Chem. A, 2022, **10**(7), 3543–3551, DOI: 10.1039/D1TA09500E.

60 M. J. Pieters, L. Bartel, C. van Helvoirt and M. Creatore, Role of the Coreactant on the Dual-Source Behavior of Lithium Hexamethyldisilazide for ALD Li-Containing Films, *J. Phys. Chem. C*, 2024, **128**(46), 19638–19647, DOI: 10.1021/acs.jpcc.4c05987.

61 V. Sallaz, S. Oukassi, F. Voiron, R. Salot and D. Berardan, Assessing the Potential of LiPON-Based Electrical Double Layer Microsupercapacitors for on-Chip Power Storage, *J. Power Sources*, 2020, **451**, 227786, DOI: 10.1016/j.jpowsour.2020.227786.

62 T. Verhelle, A. Dhara, L. Henderick, M. Minjauw, L. De Taeye, J. Meersschaut, J. Dendooven and C. Detavernier, Atomic Layer Deposition of Lithium Borate and Lithium Borophosphate for Lithium-Ion Batteries, *Chem. Mater.*, 2025, **37**(2), 687–696, DOI: 10.1021/acs.chemmater.4c02747.

63 A.-K. Landry, R. Bayzou, A. Benayad, J. Trébosc, F. Pourpoint, O. Lafon, F. L. Cras, B. P. Le Cras and R. B. Nuernberg, Unveiling the Origins of High Ionic Conductivity in Lithium Phosphorus Oxynitride Amorphous Electrolytes, *Chem. Mater.*, 2023, **35**(21), 9313–9324, DOI: 10.1021/acs.chemmater.3c02099.

64 V. Lacivita, N. Artrith and G. Ceder, Structural and Compositional Factors That Control the Li-Ion Conductivity in LiPON Electrolytes, *Chem. Mater.*, 2018, **30**(20), 7077–7090, DOI: 10.1021/acs.chemmater.8b02812.

65 R. B. Nuwayhid, D. Fontecha, A. C. Kozen, A. Jarry, S. B. Lee, G. W. Rubloff and K. E. Gregorczyk, Nanoscale, Li, Na, and K Ion-Conducting Polyphosphazenes by Atomic Layer Deposition, *Dalton Trans.*, 2022, **51**(5), 2068–2082, DOI: 10.1039/D1DT03736F.

66 S. J. Turrell, Y. Liang, T. Cai, B. Jagger and M. Pasta, Origin of Stability in the Solid Electrolyte Interphase Formed between Lithium and Lithium Phosphorus Oxynitride, *Chem. Mater.*, 2025, **37**(9), 3504–3518, DOI: 10.1021/acs.chemmater.5c00483.

67 M. Sahal, J. Guo, C. K. Chan and N. Rolston, Surface Reduction of Li2CO3 on LLZTO Solid-State Electrolyte via Scalable Open-Air Plasma Treatment, *Batteries*, 2024, **10**(7), 249, DOI: 10.3390/batteries10070249.

68 B. Put, P. M. Vereecken, J. Meersschaut, A. Sepúlveda and A. Stesmans, Electrical Characterization of Ultrathin RF-Sputtered LiPON Layers for Nanoscale Batteries, *ACS Appl. Mater. Interfaces*, 2016, **8**(11), 7060–7069, DOI: 10.1021/acsami.5b12500.

69 C. Xu, J. Tu, D. Yang, W. Xue and N. Liao, Highly Functional LiXPON (X = Al, Si, C, Sn, Y, Ta), Electrolytes for Silicon/Silicon Oxycarbide Composite All-Solid-State Batteries: First-Principles Design and Experimental Validation, *Surf. Interfaces*, 2025, **59**, 105981, DOI: 10.1016/j.surfin.2025.105981.

70 P. Xu, J. Kang, J.-B. Choi, J. Suhr, J. Yu, F. Li, J.-H. Byun, B.-S. Kim and T.-W. Chou, Laminated Ultrathin Chemical Vapor Deposition Graphene Films Based Stretchable and Transparent High-Rate Supercapacitor, *ACS Nano*, 2014, **8**(9), 9437–9445, DOI: 10.1021/nn503570j.

71 B. Pandit, B. R. Sankapal and P. M. Koinkar, Novel Chemical Route for CeO_2/MWCNTs Composite towards Highly Bendable Solid-State Supercapacitor Device, *Sci. Rep.*, 2019, **9**(1), DOI: 10.1038/s41598-019-42301-y.

72 L. Baggetto, J. F. M. Oudenhoven, T. van Dongen, J. H. Klootwijk, M. Mulder, R. A. H. Niessen, M. H. J. M. de Croon and P. H. L. Notten, On the Electrochemistry of an Anode Stack for All-Solid-State 3D-Integrated Batteries, *J. Power Sources*, 2009, **189**(1), 402–410, DOI: 10.1016/j.jpowsour.2008.07.076.

73 A. Achour, M. Chaker, H. Achour, A. Arman, M. Islam, M. Mardani, M. Boujtita, L. Le Brizoual, M. A. Djouadi and T. Brousse, Role of Nitrogen Doping at the Surface of Titanium Nitride Thin Films towards Capacitive Charge Storage Enhancement, *J. Power Sources*, 2017, **359**, 349–354, DOI: 10.1016/j.jpowsour.2017.05.074.

74 H.-Y. Xia, X.-X. Wang, G.-X. Ren, W.-W. Wang, Y.-N. Zhou, Z. Shadike, E. Hu, X.-Q. Yang, J.-Y. Zheng, X.-S. Liu and Z.-W. Fu, A New Carbon-Incorporated Lithium Phosphate Solid Electrolyte, *J. Power Sources*, 2021, **514**, 230603, DOI: 10.1016/j.jpowsour.2021.230603.